Available online at www.sciencedirect.com
SCIENCE DIRECT®
International Journal of Heat and Mass Transfer 47 (2004) 3971–3983
International Journal of HEAT and MASS TRANSFER
www.elsevier.com/locate/ijhmt

Theoretical study of evaporation heat transfer in horizontal microfin tubes: stratified flow model

H. Honda *, Y.S. Wang

Institute for Materials Chemistry and Engineering, Kyushu University, Kasuga, Fukuoka 816-8580, Japan

Received 9 September 2002; received in revised form 25 December 2003
Available online 12 May 2004

Abstract

The stratified flow model of evaporation heat transfer in helically grooved, horizontal microfin tubes has been developed. The profile of stratified liquid was determined by a theoretical model previously developed for condensation in horizontal microfin tubes. For the region above the stratified liquid, the meniscus profile in the groove between adjacent fins was determined by a force balance between the gravity and surface tension forces. The thin film evaporation model was applied to predict heat transfer in the thin film region of the meniscus. Heat transfer through the stratified liquid was estimated by using an empirical correlation proposed by Mori et al. The theoretical predictions of the circumferential average heat transfer coefficient were compared with available experimental data for four tubes and three refrigerants. A good agreement was obtained for the region of $Fr_0 < 2.5$ as long as partial dry out of tube surface did not occur.

Keywords: Evaporation; Stratified flow model; Numerical analysis; Helical microfin tube; Refrigerants

1. Introduction

Horizontal microfin tubes have been commonly used in air conditioners and refrigerators as high performance evaporator tubes. Many experimental studies on the effects of fin geometry, tube diameter, refrigerant, oil, etc. on the heat transfer and pressure drop during evaporation in the horizontal microfin tubes have been reported in the recent literature. Newell and Shah [1] and Cavallini et al. [2] have given comprehensive reviews of relevant literature. Miyara et al. [3], Murata and Hashizume [4], Kido and Uehara [5], Koyama et al. [6], Murata [7], Kandlikar and Raykoff [8], Thome et al. [9], Cavallini et al. [10], Yun et al. [11], Mori et al. [12], etc. have developed the correlations of circumferential average heat transfer coefficient α_m. While most of the correlations consisted of two terms representing the contributions of convective boiling and nucleate boiling, Murata [7] and Mori et al. [12] proposed correlations that were based on the stratified flow model. In their correlations the circumferential average heat transfer coefficient was expressed as the sum of the contributions of the upper part of tube where evaporation of thin liquid film retained in the groove between adjacent fins occurs and the lower part where convective boiling occurs within the stratified liquid. Their expression for α_m is written as

$$\alpha_m = \frac{1}{\pi}\{\varphi_s\alpha_1 + (\pi - \varphi_s)\alpha_2\} \quad (1)$$

where φ_s is the angle measured from tube top below which a stratified liquid layer exists, α_1 is the heat transfer coefficient for the upper part and α_2 is the heat transfer coefficient for the lower part. In Eq. (1), φ_s was estimated by using an empirical equation for smooth tubes and the expressions for α_1 and α_2 were determined empirically based on the available experimental data.

* Corresponding author. Tel.: +81-92-583-7787; fax: +81-92-583-7882.
E-mail address: hhonda@cm.kyushu-u.ac.jp (H. Honda).

0017-9310/$ - see front matter © 2004 Elsevier Ltd. All rights reserved.
doi:10.1016/j.ijheatmasstransfer.2004.02.027

Nomenclature

A	cross-sectional area of tube, m^2
A^*	Hamaker constant, J
B	Bond number, $(\rho_l - \rho_v)gd^2/\sigma$
Bo	boiling number, q_m/Gh_{lv}
d	diameter at fin root, m
d_e	equivalent diameter ($= \sqrt{4A/\pi}$), m
d_h	hydraulic diameter of tube ($= 4A/(S_v + S_l)$), m
d_l	hydraulic diameter of liquid space ($= 4A_l/S_l$), m
d_o	outside diameter, m
d_v	hydraulic diameter of vapor space ($= 4A_v/(S_v + S_i)$), m
Δe	sum of gravitational potential and surface energy for unit length of tube, J/m
f	friction factor
Fr	modified Froude number, $G\chi/\sqrt{d_e g\rho_v(\rho_l - \rho_v)}$
Fr_0	dimensionless quantity, $G/\sqrt{d_e g\rho_v(\rho_l - \rho_v)}$
g	gravitational acceleration, m/s^2
G	refrigerant mass velocity, $kg/m^2\,s$
h	fin height, m
h_{lv}	latent heat of evaporation, kJ/kg
n	number of fins
p	fin pitch, m
ΔP	pressure difference between liquid and vapor, Pa
Pr	Prandtl number
q	heat flux, W/m^2
r	radius of curvature of liquid surface in fin cross-section, m
r_t	radius of curvature at corner of fin tip, m
r_b	radius of curvature of liquid surface in thick film region, m
Re_v	vapor Reynolds number, $G\chi d/\mu_v$
S	perimeter length, m
T	temperature, K
ΔT_s	wall superheat ($= T_w - T_s$), K
U	velocity in axial direction, m/s
x, y	curvilinear coordinates, Fig. 2
x_a	connecting point between evaporating and non-evaporating liquid film regions, Fig. 2, m
x_b	connecting point between thin and thick film regions, Fig. 2, m
x_c	connecting point between fin flank and fin root tube surface, Fig. 2, m
x_0, x_t	connecting points between straight and round portions of fin, Fig. 2, m
X_{tt}	Martinelli parameter
X, Y	Cartesian coordinates, Fig. 2
z	vertical height measured from stratified liquid surface, Fig. 1

Greek symbols

α	heat transfer coefficient, $W/m^2\,K$
β	angle, Fig. 2, deg
γ	helix angle of groove, deg
δ	liquid film thickness, m
ε	angle, Fig. 2, deg
ε_a	surface area enhancement compared to a smooth tube, $S/\pi d$
ζ	wettability angle, deg
θ	fin half tip angle, deg
λ	thermal conductivity, W/m K
μ	dynamic viscosity, Pa s
ν	kinematic viscosity, m^2/s
ρ	density, kg/m^3
σ	surface tension, N/m
φ	angle measured from tube top, deg
χ	mass quality
ω	angle, Fig. 1, deg

Subscripts

a	boundary of non-evaporating and evaporating film regions
b	boundary of thin and thick film regions
c	coolant side
i	vapor–liquid interface
l	liquid
m	circumferential average value
p	average value for fin cross-section
r	mid-point at fin root
s	saturation or stratified liquid
v	vapor
w	wall
φ	average value for fin cross-section at $\varphi = \varphi$
1	region 1
2	region 2

Mori et al. [12] compared the predictions of 10 correlations with available experimental data for nine refrigerants and 26 tubes. The best agreement (mean absolute deviation of 19% for 1265 data points) was obtained by their correlation.

The factors leading to enhanced evaporation in the horizontal microfin tubes are considered to be evaporation of thin liquid film that occurs on the fin surface, enhanced turbulence in the thick liquid film and surface area increase due to finning. However, the mechanism of heat transfer enhancement is not well understood. At present, there exists no definite principle to choose relevant dimensionless groups for describing the fin geometry effect and the physical meaning of geometrical

parameters adopted in the proposed correlations are not so clear.

The objective of the present study is to develop a theoretically based prediction method for heat transfer during evaporation in helically grooved, horizontal microfin tubes. Wang et al. [13] proposed the annular flow model and the stratified flow model of film condensation in horizontal microfm tubes. Generally, the stratified flow model gave a higher prediction of the circumferential average heat transfer coefficient at low mass velocities, whereas the annular flow model gave a higher prediction at high mass velocities. Comparison of the predictions of these models and five previously proposed correlations with available experimental data for five refrigerants and six tubes revealed that a good agreement (r.m.s. deviation of 14.3% for 440 data points), much better than those of the correlations, was obtained by the theoretical model if the higher of the two theoretical predictions were adopted as the calculated value [14]. In this paper, the stratified flow model of evaporation heat transfer in horizontal microfin tubes is developed based on the theoretical treatment which is basically the same as the case of condensing stratified flow. For the region above the stratified liquid, the meniscus profile in the groove between adjacent fins was determined by a force balance between the gravity and surface tension forces. The thin film evaporation model for a well wetting liquid, developed by Potash and Wayner [15] and applied later to the analysis of groove heat pipes by Stephan and Busse [16], Khrustalev and Faghri [17] and Ha and Peterson [18], is applied with rigorous boundary conditions to calculate heat transfer in the thin film region of the meniscus. For the heat transfer thorough the stratified liquid, the empirical equation developed by Mori et al. [12] is adopted. The predictions of α_m by the theoretical model are compared with available experimental data for four tubes and three refrigerants.

2. Analysis

2.1. Stratified flow model

Fig. 1 shows the physical model of stratified liquid flow in a helically grooved, horizontal microfin tube. The shape of stratified liquid is assumed to be a circular arc centered at O_1. The angle φ is measured from the top of tube. The coordinate z is measured vertically upward from the liquid vapor interface at $\varphi = \varphi_s$. The tube surfaces at the angular portions $0 \leqslant \varphi \leqslant \varphi_s$ and $\varphi_s \leqslant \varphi \leqslant \pi$ are denoted as region 1 and region 2, respectively.

The profile of stratified liquid is estimated by the combination of Taitel and Dukler model [19] for the void fraction modified by Wang et al. [13] and the model of interface configuration proposed by Brauner et al. [20]. The basic equation for stratified flow is written as

$$f_v \frac{\rho_v U_v^2}{2} \frac{S_v}{A_v} - f_l \frac{\rho_l U_l^2}{2} \frac{S_l}{A_l} + f_i \frac{\rho_v U_v^2}{2} \left(\frac{S_i}{A_v} + \frac{S_i}{A_l} \right) = 0 \qquad (2)$$

where f_v and f_l are the friction factors in regions 1 and 2, respectively, f_i is the interfacial friction factor, ρ_v and ρ_l are the densities of vapor and condensate, respectively, U_v and U_l are the velocities of vapor and liquid, respectively, A_v and A_l are the cross-sectional areas of the vapor space and liquid space, respectively, S_v and S_l are the perimeter lengths of regions 1 and 2, respectively, and S_i is the perimeter length of the interface. The values f_v and f_l are estimated by an empirical equation for the internally finned tubes developed by Carnavos [21]. Thus they are respectively given by the following equations:

$$f_v = 0.046 \left(\frac{\rho_v d_v U_v}{\mu_v} \right)^{-0.2} \left(\frac{A}{A_n} \right)^{0.5} (\sec \gamma)^{0.75} \qquad (3)$$

$$f_l = 0.046 \left(\frac{\rho_l d_l U_l}{\mu_l} \right)^{-0.2} \left(\frac{A}{A_n} \right)^{0.5} (\sec \gamma)^{0.75} \qquad (4)$$

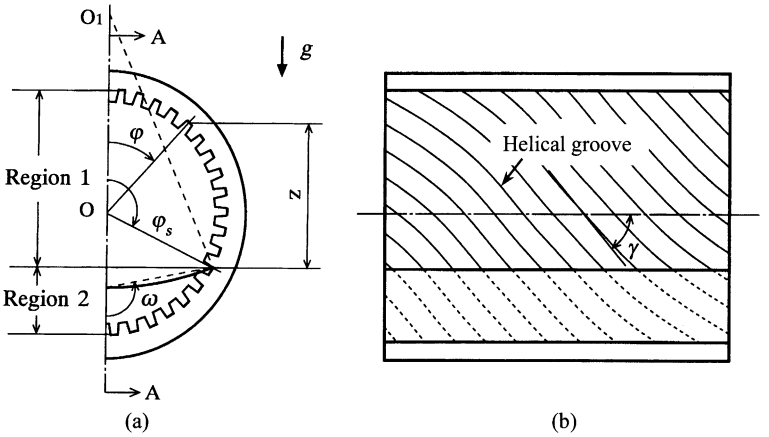

Fig. 1. Physical model of stratified flow in a horizontal microfin tube. (a) Tube cross-section and (b) A–A cross-section.

The f_i is given by

$$f_i = 0.046\left(\frac{\rho_v d_v U_v}{\mu_v}\right)^{-0.2} \tag{5}$$

where d_v and d_l are the equivalent diameters of the vapor space and liquid space given by $d_v = 4A_v/(S_v + S_i)$ and $d_l = 4A_l/S_l$, respectively, A is the actual cross-sectional area of tube, A_n is the nominal cross-sectional area based on the fin root diameter d, γ is the helix angle of the groove and μ_l and μ_v are the dynamic viscosities of liquid and vapor, respectively. The expressions for the other parameters are as follows: $U_v = GA\chi/\rho_v A_v$, $U_l = GA(1-\chi)/\rho_l A_l$, $S_v = \varepsilon_a d\varphi_s$, $S_l = \varepsilon_a d(\pi - \varphi_s)$, $S_i = d\sin\varphi_s(\pi - 2\omega)/\sin(2\omega)$,

$$A_l = \frac{d^2}{4}\left[\frac{A}{A_n}(\pi - \varphi_s) + \frac{\sin(2\varphi_s)}{2} + \sin^2\varphi_s\frac{\pi - 2\omega + \sin(4\omega)/2}{\sin^2(2\omega)}\right]$$

and

$$A_v = \pi d^2/4 - A_l,$$

where G is the refrigerant mass velocity, ε_a is the surface area enhancement as compared to a smooth tube with diameter d, ω is the angle shown in Fig. 1 and χ is the mass quality.

Following Brauner et al. [20], it is assumed that the sum of gravitational potential and surface energy of the stratified flow Δe takes a minimum value. The Δe is given by

$$\Delta e = \frac{1}{8}(\rho_l - \rho_v)gd^3\left[\sin^3\varphi_s(\cos(2\omega) + \cot\varphi_s) \times \frac{\pi - 2\omega + \sin(4\omega)/2}{\sin^2(2\omega)} + \frac{2}{3}\sin^3\varphi_s^p + \frac{8}{B}\left\{\sin\varphi_s \times \frac{\pi - 2\omega}{\sin(2\omega)} - \sin\varphi_s^p + \cos\zeta(\varphi_s - \varphi_s^p)\right\}\right] \tag{6}$$

where $B = (\rho_l - \rho_v)gd^2/\sigma$ is the Bond number, σ is the surface tension, φ_s^p is the value of φ_s for a plane interface ($\omega = \pi/2$), and ς is the wettability angle. It is further assumed that $\zeta = 0$ for refrigerants. For given conditions of d, G and χ, φ_s and ω are obtained by solving Eqs. (2) and (6) iteratively.

2.2. Liquid film profile in fin cross-section

Fig. 2(a) shows the liquid film profiles of a well wetting liquid in the fin cross-section in region 1. The fin profile is assumed by a trapezoid with a round corner at the fin tip. The fin height and fin pitch are h and p, respectively, and the fin half tip angle is θ. The radius of curvature at the corner of fin tip is r_t. The coordinate x is measured along the fin surface from the center of fin tip and y is measured vertically outward from the fin surface. The X and Y are the Cartesian coordinates measured horizontally and vertically upward from the mid-point at fin root, respectively. The connecting points between the straight and round portions at the fin tip are x_0 and x_t. The coordinate at the fin root is x_c, and that at the mid-point between adjacent fins is x_r. Liquid is pulled up above the level of stratified liquid by the capillary effect and evaporates on the fin surface. The effect of vapor shear force on the liquid flow is assumed to be negligible. The liquid film in the fin cross-section is divided into three regions: the non-evaporating film region, the thin film region with a high evaporation rate and the thick film region with a relatively low evaporation rate. In the thick film region, the effects of viscous and gravity forces on the meniscus profile are assumed to be negligible as compared to the capillary effect. Thus the meniscus profile is approximated by a circular arc with radius r_b. The assumption of constant r_b is correct when the pressure difference between the two ends of the meniscus ΔP_g caused by the gravity effect is sufficiently smaller than the absolute value of $\Delta P_b = -\sigma/r_b$ (i.e., pressure difference between vapor and liquid caused by the capillary effect). The value of ΔP_g is largest at $\varphi = 90°$. Representing the meniscus profile by a circular arc which touches the fin flank at $x = x_t$, the pressure ratio $\Delta P_g/|\Delta P_b|$ at $\varphi = 90°$ is written as

$$\frac{\Delta P_g}{|\Delta P_b|} = \frac{(\rho_l - \rho_g)g[p - 2(x_0 + r_0)]^2}{2\sigma\cos\theta} \tag{7}$$

Substitution of experimental conditions for tubes A–D cited in the next section revealed that the maximum value of $\Delta P_g/|\Delta P_b| = 0.19$ was obtained for tube D. Thus the assumption of circular meniscus is acceptable for the experimental data cited in this paper.

The liquid flow along the groove is driven by the sum of the gradient of ΔP_b and the component of gravity force parallel to the groove. Since the liquid flow rate depends on the evaporation rate in region 1, which is determined by solving Eqs. (9)–(23) described in the next section, an iterative procedure is required to obtain a converged solution for liquid flow along the groove. If the viscous force is assumed to be much smaller than the gravity force, ΔP_b, is obtained from the static force balance between the capillary and gravity forces as follows:

$$\Delta P_b = -\frac{\sigma}{r_b} = -(\rho_l - \rho_v)gz = -\frac{(\rho_l - \rho_v)gd}{2}(\cos\varphi - \cos\varphi_s) \tag{8}$$

Eq. (8) is used in the present analysis.

Fig. 2(b)–(d) shows three cases of liquid film profile that corresponds to Cases A, B and C in Fig. 2(a),

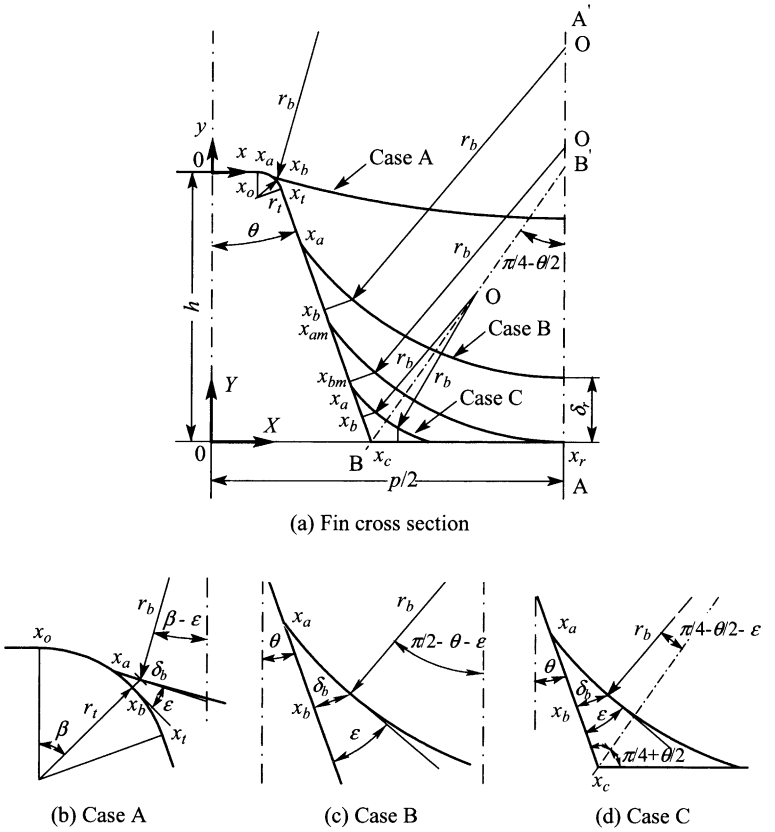

Fig. 2. Liquid film profiles in fin cross-section of region 1.

respectively. The connecting point between the non-evaporating film region and the evaporating film region is denoted as x_a, and the connecting point between the thin film region and the thick film region is denoted as x_b. In Fig. 2(b) for Case A, x_a is located in between x_0 and x_t. In Fig. 2(c) for Case B, x_a is located in between x_t and x_{am}, where x_{am} denotes the value of x_a at which the liquid film thickness at $x = x_r$, δ_r, is equal to 0. For Cases A and B, the liquid film profile is symmetrical with respect to $X = p/2$. In Fig. 2(d) for Case C, x_a is located in between x_{am} and x_r. For this case the liquid film profile is symmetrical with respect to the line B–B′ and the non-evaporating film and thin film regions are formed on both the fin flank and fin root tube surfaces.

2.3. Liquid film profile in thin film region

The liquid in the thick film region is driven by the surface tension induced pressure gradient toward the thin film region and evaporates. Since $d \gg p$, the effect of pressure gradient along the groove on the liquid flow in the x region is neglected. The effect of gravity is also neglected. The momentum equation in the x-direction is written as

$$\mu_l \frac{d^2u}{dy^2} = \frac{d\Delta P}{dx} \tag{9}$$

where u is the velocity components in the x-direction and ΔP is the pressure difference between the liquid and vapor. The boundary conditions are

$$u = 0 \quad \text{at } y = 0 \tag{10}$$

$$du/dy = 0 \quad \text{at } y = \delta \tag{11}$$

where δ is the local film thickness. The solution for u is given by

$$u = \frac{1}{2\mu_l}\frac{d\Delta P}{dx}(y^2 - 2\delta y) \tag{12}$$

The ΔP in Eq. (12) is given by the sum of the disjoining pressure $-A^*/6\pi\delta^3$, the capillary pressure σ/r and the momentum term $q^2/\rho_v h_{lv}^2$ as follows:

$$\Delta P = -\frac{A^*}{6\pi\delta^3} + \frac{\sigma}{r} + \frac{q^2}{\rho_v h_{lv}^2} \tag{13}$$

where A^* is the Hamaker constant, r is the radius of curvature of liquid surface in the fin cross-section, q is the local heat flux and h_{lv} is the latent heat of

evaporation. The value of A^* is estimated by using the following approximation proposed by Israelachvili [22].

$$A^* \approx 2.1 \times 10^{-18}\sigma \tag{14}$$

The expression for r is given by

$$\frac{1}{r} = -\frac{\mathrm{d}^2\delta/\mathrm{d}x^2}{\{1+(\mathrm{d}\delta/\mathrm{d}x)^2\}^{3/2}} \quad \text{for } x_t \leqslant x \leqslant x_r \tag{15a}$$

and

$$\frac{1}{r} = \frac{\frac{1}{r_0} + \left(\frac{2}{r_0^2} + \frac{\delta}{r_0^3}\right)\delta + \frac{2}{r_0}\left(\frac{\mathrm{d}\delta}{\mathrm{d}x}\right)^2 - \left(1+\frac{\delta}{r_0}\right)\left(\frac{\mathrm{d}^2\delta}{\mathrm{d}x^2}\right)}{\left\{\left(1+\frac{\delta}{r_0}\right)^2 + \left(\frac{\mathrm{d}\delta}{\mathrm{d}x}\right)^2\right\}^{3/2}}$$

$$\text{for } x_0 \leqslant x \leqslant x_t \tag{15b}$$

Since δ is very small, a linear temperature drop is assumed across the condensate film. Thus q is given by

$$q = \frac{k_l(T_w - T_i)}{\delta} \tag{16}$$

where k_l is the thermal conductivity of liquid, T_w is the wall temperature and T_i is the temperature at liquid surface. Following Wayner [23], and assuming that the accommodation coefficient is equal to unity, q is also written as

$$q = \left(\frac{2}{\pi R_v T_i}\right)^{1/2} \frac{\rho_v h_{lv}^2}{T_i}\left(T_i - T_s + \frac{T_s}{\rho_l h_{lv}}\Delta P\right) \tag{17}$$

where R_v is the gas constant.

The q is related to u by the following equation:

$$q = \rho_l h_{lg}\frac{\mathrm{d}}{\mathrm{d}x}\int_0^\delta u\,\mathrm{d}y \tag{18}$$

Combining Eqs. (12), (13), (16) and (18) yields

$$\frac{1}{3\nu_l}\frac{\mathrm{d}}{\mathrm{d}x}\left[\delta^3\frac{\mathrm{d}}{\mathrm{d}x}\left\{-\frac{A^*}{6\pi\delta^3} + \frac{\sigma}{r} + \frac{q^2}{\rho_v h_{lv}^2}\right\}\right] = \frac{k_l(T_w - T_i)}{h_{lv}\delta} \tag{19}$$

The boundary conditions are

$$\delta = \delta_a \quad \text{and} \quad \mathrm{d}(1/r)/\mathrm{d}x = 0 \qquad \text{at } x = x_a \tag{20}$$

$$\mathrm{d}\delta/\mathrm{d}x = \tan\varepsilon \quad \text{and} \quad r = -r_b \qquad \text{at } x = x_b \tag{21}$$

where δ_a is the thickness of non-evaporating liquid film and ε is the angle shown in Fig. 2(b)–(d). The second equation of the boundary conditions (20) indicates that $\mathrm{d}\Delta P/\mathrm{d}x = 0$ at $x = x_a$. The boundary conditions (21) require that the thin film is smoothly connected with the meniscus region. The value of δ_a is obtained by putting $q = 0$ in Eqs. (13), (16) and (17) and then eliminating ΔP and T_i from the resulting equations as follows:

$$\delta_a = \left[\frac{6\pi}{A^*}\left\{\frac{\rho_l h_{lv}(T_w - T_s)}{T_v} + \frac{\sigma}{r_a}\right\}\right]^{-1/3} \tag{22}$$

where r_a is the value of r at $x = x_a$. Due to the geometrical condition, the value of r_b, for Cases A–C are respectively given by the following equations:

$$r_b = \frac{p/2 - r_0 - (r_0 + \delta_b)\sin\varphi}{(\sin\varphi - \varepsilon)} \quad \text{for Case A} \tag{23a}$$

$$r_b = \frac{1}{\cos(\theta+\varepsilon)}\left\{\frac{p}{2} - \left[x_0 + r_0\left(\frac{\pi}{2} - \theta\right) + (x_b - x_t)\sin\theta\right] - \delta_b\cos\theta\right\} \quad \text{for Case B} \tag{23b}$$

$$r_b = \frac{1}{\tan\left(\frac{\pi}{4} - \frac{\theta}{2} - \varepsilon\right)}\left\{\frac{\sin\left(\frac{\pi}{4} + \frac{\theta}{2}\right)}{\sin\left(\frac{3\pi}{4} - \frac{\theta}{2} - \varepsilon\right)} \times \left[x_c + \frac{r_r}{\tan\left(\frac{\pi}{4} + \frac{\theta}{2}\right)} - x_b + \frac{\delta_b}{\tan\varepsilon}\right] - \frac{\delta_b}{\sin\varepsilon}\right\} \quad \text{for Case C} \tag{23c}$$

It should be mentioned here that the length of thin film region $x_b - x_a$ is not given a priori. Thus a physically meaningful condition is required to determine the value of $x_b - x_a$.

The solution of Eq. (19) subject to the boundary conditions (20) and (21) was obtained numerically by a finite difference scheme. In the numerical calculation, the unsteady term $\rho_l\partial\delta/\partial t$ was added to the left-hand side of Eq. (19) and the solution was obtained as the steady-state solution of an unsteady liquid flow subject to an arbitrary initial distribution of δ. The calculation was started assuming the values of x_a and $x_a - x_b$, and the initial distribution of δ. A non-uniform grid of $\Delta x_j = \Delta x_0 + a_j^2$ was adopted for x with $\Delta x_0 = 10^{-12}$–10^{-11} m and the total number of grid points of 101. The value of a was changed depending on $x_a - x_b$. At the beginning of numerical calculation, a small value was assumed for the time step $\Delta\tau_k$ and it was increased with time. Calculation was continued until the convergence criteria $|1 - \delta_{j,k-1}/\delta_{j,k}| < 10^{-3}$ and $|\rho_l h_{lg}(\delta_{j,k} - \delta_{j,k-1})/\Delta\tau_k q_{j,k}| < 10^{-3}$ were satisfied. As seen from Eq. (22), δ_a is a function of r_a. Since r_a was not known a priori, calculation was started with an appropriate assumption of r_a. Then the calculation was repeated several times using an iterative procedure to obtain the solution in which the assumed and calculated values of r_a agreed within 0.1%. It should be mentioned here that the value of ε in Eq. (21) is arbitrary. Preliminary numerical calculations were conducted assuming $\varepsilon = 15°$, 30° and 45° to determine the appropriate value of ε. The numerical results showed that the liquid film profiles for $\varepsilon = 30°$ and 45° were virtually the same. Thus, systematic calculation was conducted assuming $\varepsilon = 30°$.

For a fixed value of x_a, calculation was started assuming a very small value of $x_b - x_a$. Then the calculation was repeated increasing the value of $x_b - x_a$. Numerical results showed that there existed a maximum value $(x_b - x_a)_{max}$ below which a continuous distribution of δ was obtained. Thus, one more condition is required to determine a physically meaningful solution among a family of solutions with fixed x_a and different $x_b - x_a$. It is well known that a droplet of well wetting liquid continues to spread on an adiabatic surface. This indicates that the solution for $(x_b - x_a)_{max}$ is the physically meaningful solution for the evaporating liquid film. Thus the solution for $(x_b - x_a)_{max}$ was adopted in this paper. The value of x_a was changed in small steps between x_0 and x_c. The value of x_{am} (defined as the value of x_a at which $\delta_r = 0$) was determined by the interpolation of the solutions for different x_a.

2.4. Wall temperature and heat transfer coefficient

For region 1, the average heat transfer coefficient for fin cross-section α_p is defined on the projected area basis as

$$\alpha_p = \frac{2}{p(T_w - T_s)} \int_{x_a}^{x_r} q \, dx \tag{24}$$

In Eq. (24), q in the thick film region was obtained by assuming a radial conduction through the liquid film centered at point O in Fig. 2(a). The α_p is related to the angle φ through the value of r_b given by Eq. (23). Thus the average heat transfer coefficient for fin cross-section at φ–φ, α_p, is also given by Eq. (24).

The average heat transfer coefficient for region 1, α_1, is defined on the projected area basis as

$$\begin{aligned}\alpha_1 &= \frac{1}{\varphi_s} \int_0^{\varphi_s} \alpha_\varphi \, d\varphi \\ &= \frac{2}{p\varphi_s(T_{wl} - T_s)} \int_0^{\varphi_s} \int_{x_a}^{x_r} q \, dx \, d\varphi \end{aligned} \tag{25}$$

The heat transfer coefficient in region 2, α_2, was assumed to be uniform. The α_2 was estimated by using the empirical equation developed by Mori et al. [12] as follows:

$$\begin{aligned}\alpha_2 = {} & 0.023 \varepsilon_a^{1.3} \frac{k_l}{d_e} \left[\frac{G(1-\chi)d_e}{\mu_l} \right]^{0.8} Pr_l^{0.4} \\ & \times \left[1 + C_f \left(\frac{1}{x_{tt}} \right)^{0.93} + C_b Bo^{0.8} \right] \end{aligned} \tag{26}$$

where

$$\begin{aligned} C_f = {} & 1.47 \times 10^4 \left(\frac{h}{d_e} \right)^{-0.4} \left(\frac{t}{d_e} \right)^{0.8} \left(\frac{Gd_e}{\mu_l} \right)^{-0.65} \\ & \times \left[1 - 0.93 \exp\left(-5 \times 10^{-4} \frac{Gd_e}{\mu_l} \right) \right] \left(\frac{\rho_v}{\rho_l} \right)^{0.45}, \end{aligned}$$

$$C_b = 1.58 \times 10^3 \left[1.6 + 0.063 \left(\frac{1}{X_{tt}} \right)^{0.3} \left(\frac{Gd_e}{\mu_l} \right)^{0.3} \right]^{-1},$$

$$X_{tt} = \left(\frac{1-\chi}{\chi} \right)^{0.9} \left(\frac{\rho_v}{\rho_l} \right)^{0.5} \left(\frac{\mu_l}{\mu_v} \right)^{0.1}$$

is the Martinelli parameter, $Bo = q_m/Gh_{lv}$ is the boiling number and q_m is the circumferential average heat flux.

The wall superheat $(T_{wn} - T_s)$ and the heat flux q_n in region $n(= 1, 2)$ are obtained from

$$\begin{aligned} q_n &= \left\{ \frac{1}{\alpha_n} + \frac{d}{2k_w} \ln\left(\frac{d_o}{d} \right) \frac{d}{\alpha_o d_o} \right\}^{-1} (T_h - T_s) \\ &= \alpha_n (T_{wn} - T_s) \end{aligned} \tag{27}$$

where d_o is the tube outside diameter, k_w is the thermal conductivity of tube wall, α_0 is the outside heat transfer coefficient and T_{wn} is the inside tube wall temperature in region n. Then the circumferential average heat transfer coefficient α_m is obtained from

$$\alpha_m = q_m/(T_s - T_{wm}) \tag{28}$$

where T_{wm} is the circumferential average wall temperature. The q_m and T_{wm} are respectively defined as follows:

$$q_m = \{\varphi_s q_1 + (\pi - \varphi_s) q_2\}/\pi \tag{29}$$

$$T_s - T_{wm} = \{\varphi_s (T_s - T_{w1}) + (\pi - \varphi_s)(T_s - T_{w2})\}\pi \tag{30}$$

3. Numerical results

Numerical calculations were conducted for specific experimental conditions reported by Yu et al. [24], Miyara et al. [25] and Del Col et al. [26]. The fin and tube dimensions of tubes A–D used in these experiments are summarized in Table 1. For each tube, the average fin dimensions were obtained from the enlarged photograph of tube cross-section. The test fluid was R22 and R134a for tube A, R410A for tubes B and C, and R22 for tube D. All test tubes were heated by hot water flowing counter-currently in the annular space around the test tube. For tubes A–C, which consisted of 6 or 12 sub-sections, the local wall temperatures at the top, side(s) and bottom of each sub-section were measured by thermocouples and their arithmetic mean value was adopted to calculate the sectional-average heat transfer coefficient α_m. For tube D, α_m was estimated by using the Wilson plot method. In the data reduction, the physical properties of refrigerants were obtained from the REFPROP Version 6.0 [27]. The uncertainty in the measured α_m is estimated to be within 15%.

Fig. 3(a) and (b) shows examples of the distribution of q along the fin surface for the combination of tube A and R22 that correspond to Cases B and C in Fig. 2, respectively. In each figure, five solutions for fixed x_a and

Table 1
Fin and tube dimensions

			Tube designation			
			A	B	C	D
Outside diameter	d_o	mm	10.0	7.0	7.0	15.88
Fin root diameter	d	mm	8.48	6.50	6.49	14.85
Number of fins	n	–	60	50	60	73
Helix angle	γ	deg	18.0	18.0	18.0	21.5
Fin pitch[a]	p	mm	0.42	0.39	0.34	0.64
Fin height	h	mm	0.16	0.21	0.19	0.38
Fin half tip angle[a]	θ	deg	19.9	19.5	13.1	20.8
Curvature radius at corner of fin tip[a]	r_o	mm	0.015	0.008	0.030	0.04
Length of flat portion at fin tip[a]	x_o	mm	0.027	0.019	0.018	0.02
Area enhancement ratio	ε_a	–	1.52	1.71	1.78	1.76
Authors			Yu et al.	Miyara et al.	Miyara et al.	Del Col et al.

[a] Dimension in a cross-section normal to groove.

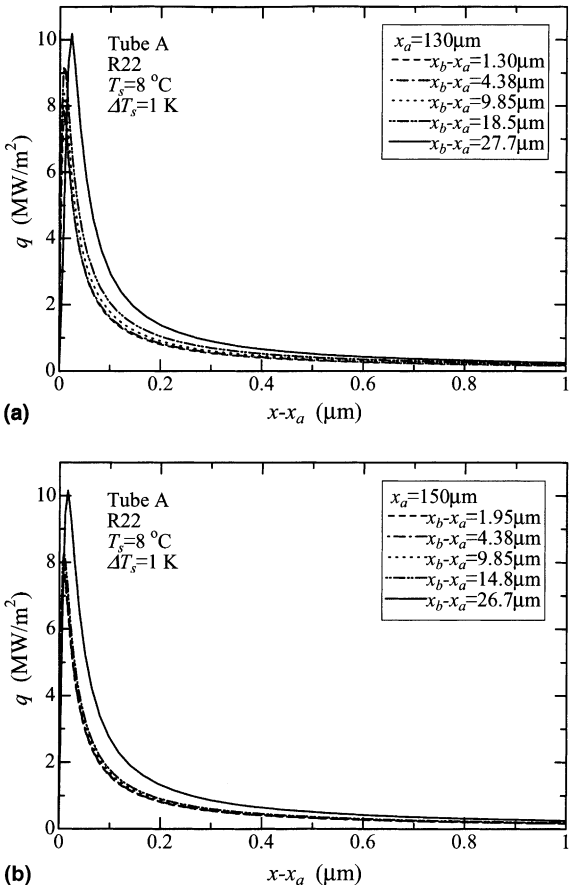

Fig. 3. Distribution of q along fin surface.

different $x_b - x_a$ are presented. Generally, q increases sharply with increasing $x - x_a$ and takes a maximum value at $x - x_a \approx 10^{-8}$–2×10^{-8} m. Then it decreases first sharply, and then gradually, with increasing $x - x_a$. Thus, intense evaporation occurs only at a very short length on the fin cross-section. The solid line in Fig. 3 shows the solution for $x_b - x_a = (x_b - x_a)_{max}$. This solution gives the highest q except for a small region near $x - x_a = 0$.

Fig. 4(a) and (b) shows the distributions of ΔP along the fin surface that correspond to Fig. 3(a) and (b), respectively. The ΔP takes the smallest value ΔP_a at $x = x_a$. Due to the boundary condition, $d\Delta P/dx = 0$ at $x = x_a$. However, ΔP increases sharply after a very short length (about 10 nm). The slope decreases with increasing $x - x_a$ and ΔP approaches $\Delta P_b = -\sigma/r_b$ in the region of $(x - x_a) > (x_b - x_a)/3$. As described previously, ΔP consists of three terms on the right-hand side of Eq. (13). Comparison of these terms reveals that $q^2/\rho_v h_{lv}^2$ is much smaller than $A^*/6\pi\delta^3$ and $|\sigma/r|$. The $A^*/6\pi\delta^3$ is largest near $x = x_a$ but it decreases very rapidly with increasing $x - x_a$ in the region of $x - x_a < 0.02$ μm and takes a value smaller than 0.1% of $|\sigma/r|$ for $x - x_a > 0.2$ μm. It is relevant to note here that $\delta_a = 1.07$ nm and $|\sigma/r_a|/(A^*/6\pi\delta_a^3) = 0.080$ for the case of $x_b - x_a = 27.7$ μm shown in Figs. 3(a) and 4(a). The $|\sigma/r|$ also decreases with increasing $x - x_a$ but the slope is much smaller than $A^*/6\pi\delta^3$. The above results indicate that the disjoining pressure is very important only in the region close to $x = x_a$ where the film thickness is of the order of several molecules. Comparison of the solutions for different $x_b - x_a$ reveals that ΔP_a is almost constant irrespective of $x_b - x_a$. It is seen from Fig. 5 that the change in ΔP_b is also small. Since the vapor pressure is constant, $\Delta P_b - \Delta P_a$ is equal to the pressure drop due to liquid flow over the thin film region. If the distributions of δ for different $x_b - x_a$ are similar to each other, $\Delta P_b - \Delta P_a$ should increase with increasing $x_b - x_a$, because the frictional pressure drop is proportional to $x_b - x_a$. According to the numerical results, however, $\Delta P_b - \Delta P_a$ changes slightly with $x_b - x_a$. This indicates that the frictional pressure drop is kept in equilibrium with the

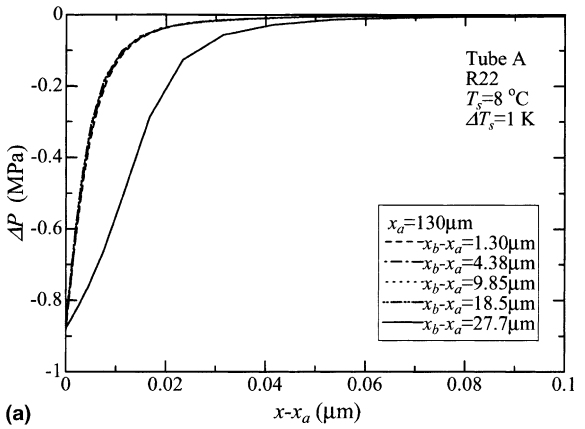

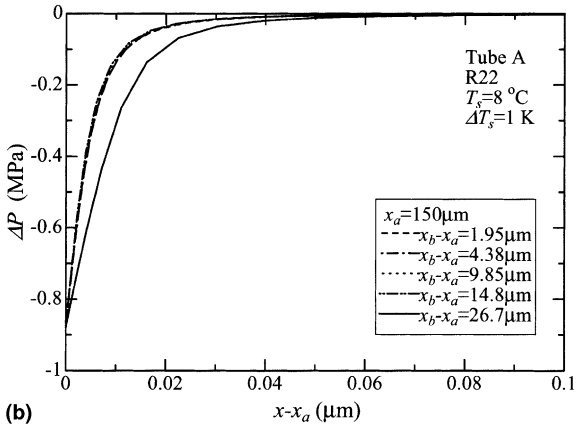

Fig. 4. Distribution of ΔP along fin surface.

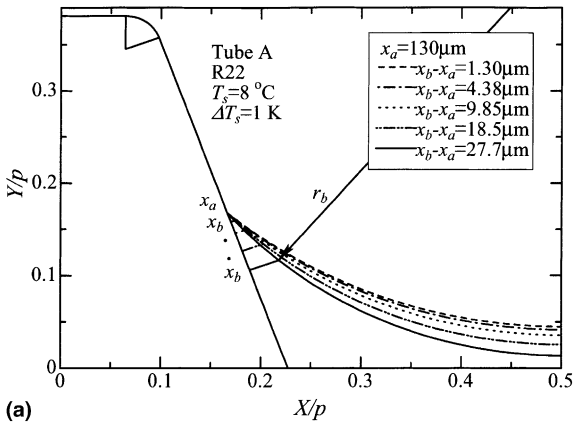

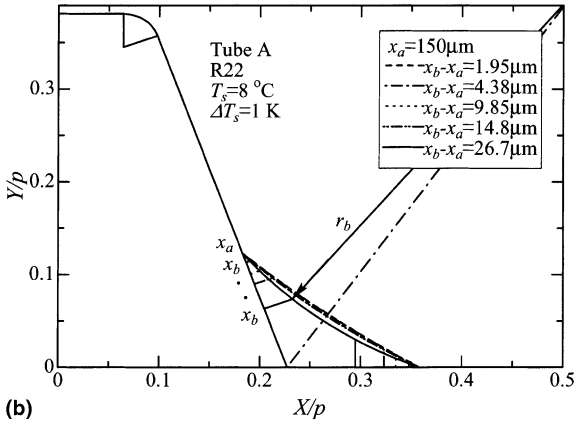

Fig. 5. Liquid film profile on fin cross-section.

pressure drop determined by the boundary conditions at $x = x_a$ and x_b through the change in the distribution of δ along x. However, this equilibrium can not be maintained beyond $(x_b - x_a)_{max}$. Thus, a continuous liquid film is not obtained beyond this limit.

Fig. 5(a) and (b) shows the liquid film profiles that correspond to Fig. 3(a) and (b), respectively. In Fig. 5(a) for Case B, the thin film region is formed only on the fin flank. In Fig. 5(b) for Case C, on the other hand, the thin film region is formed on both the fin flank and fin root tube surface. For both cases, r_b decrease slightly as $x_b - x_a$ increases.

Fig. 6(a) and (b) shows the variations of α_p and $-\Delta P_b$ with $x_b - x_a$ that correspond to Fig. 3(a) and (b), respectively. The α_p is almost unchanged in the region of $x_b - x_a < 5$ μm. Then it increases first gradually, and then sharply, with increasing $x_b - x_a$. The $-\Delta P_b$ also increase first gradually, and then sharply, with increasing $x_b - x_a$. Comparison of Fig. 6(a) and (b) reveals that α_p is much higher for Fig. 6(b), which is due to the difference in the liquid film profile shown in Fig. 5(a) and (b).

Fig. 7 shows an example of the circumferential distribution of α_φ. In Fig. 7, the ranges of φ that correspond to Cases A, B and C in region 1, and region 2 are also shown. The α_φ takes a large value for Case C. It increases gradually with increasing φ and takes a maximum value at $\varphi = 38.4°$ which corresponds to the transition point between Cases B and C. Then α_φ decreases first sharply, and then gradually, with further increasing φ. The α_φ shows a bend at $\varphi = 57.9°$ which corresponds to the transition point between Cases A and B. Then α_φ decreases sharply near $\varphi = \varphi_s$ and takes a constant value in region 2 ($\varphi_s \leqslant \varphi \leqslant \pi$).

Figs. 8–15 show comparisons of the theoretical predictions of α_m with available experimental data [24–26]. Since the value of α_0 was not available in the experimental data, the assumption of $q_1 = q_2 = q_m$ was adopted in the numerical calculation, where q_m denotes the measured sectional-average heat flux. This means that $\alpha_1, \alpha_2 \gg \alpha_o$ was assumed in Eq. (27). In Figs. 8–15, the Mori et al. [12] correlation is also shown for comparison. Figs. 8 and 9 show the cases of Tube A with R22 at $G = 115.3$ and 306.1 kg/m^2 s, respectively. The

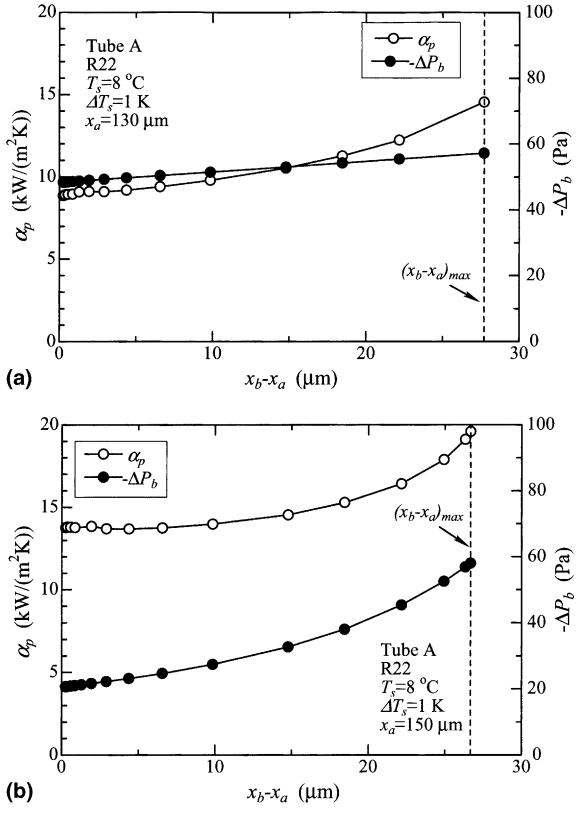

Fig. 6. Variations of α_p and $-\Delta P_b$, with $x_b - x_a$.

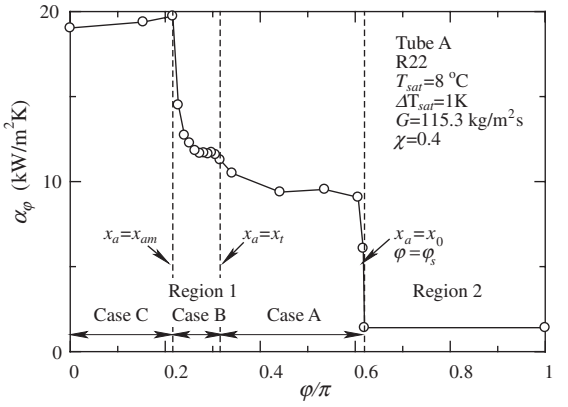

Fig. 7. Circumferential distribution of α_φ.

agreement between the measured and calculated values is generally good at $G = 115.3$ kg/m^2 s. The theoretical prediction gives a lower value than the measurement at $G = 306.1$ kg/m^2 s and the difference increases as χ increases. For this case, the measured value shows a sudden drop at $\chi > 0.8$. This is probably due to the partial dry out of the tube surface that is not taken into account

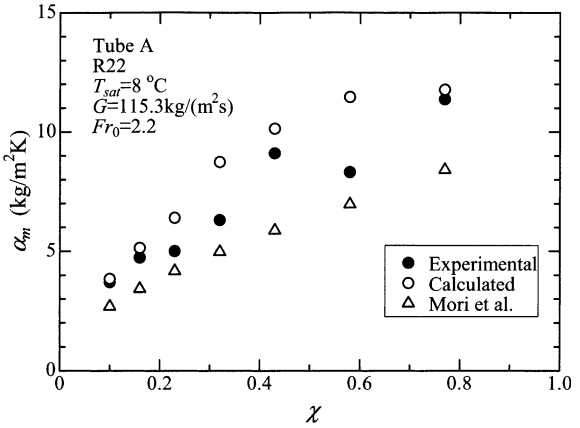

Fig. 8. Comparison of measured and predicted α_m values.

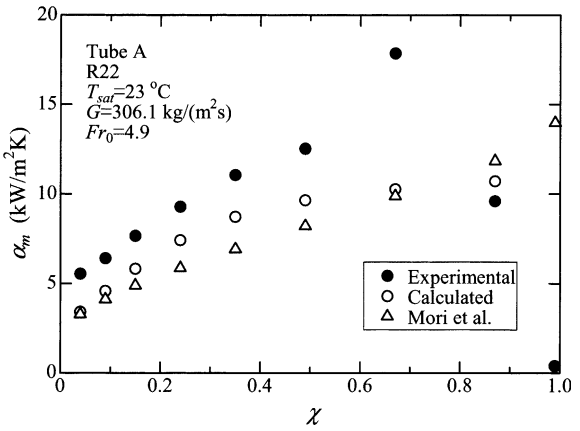

Fig. 9. Comparison of measured and predicted α_m values.

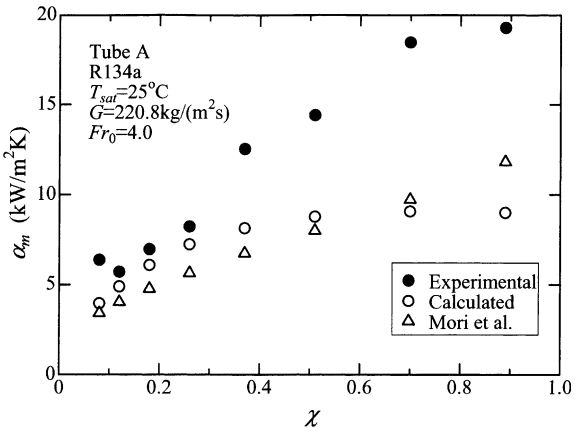

Fig. 10. Comparison of measured and predicted α_m values.

in the theoretical analysis. Fig. 10 shows the case of tube A with R134a at $G = 220.8$ kg/m^2 s. The agreement is

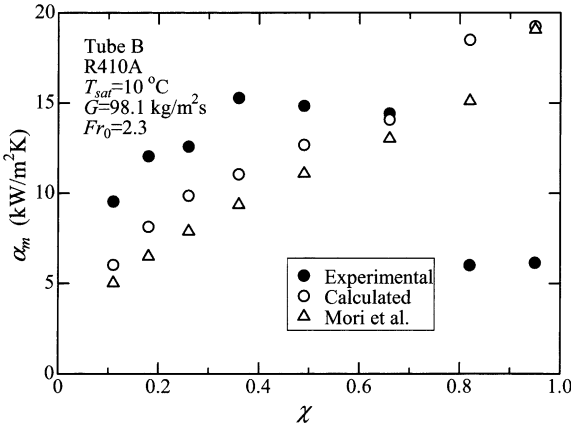

Fig. 11. Comparison of measured and predicted α_m values.

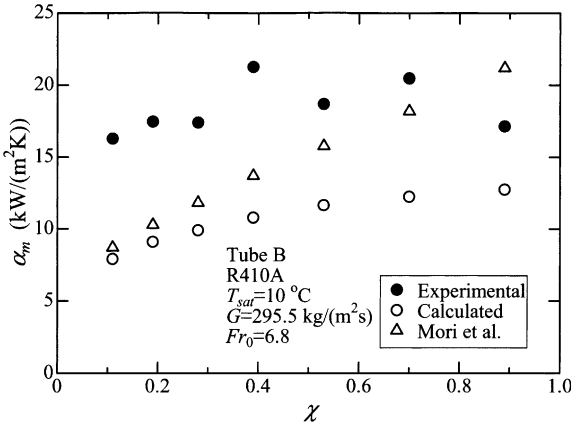

Fig. 12. Comparison of measured and predicted α_m values.

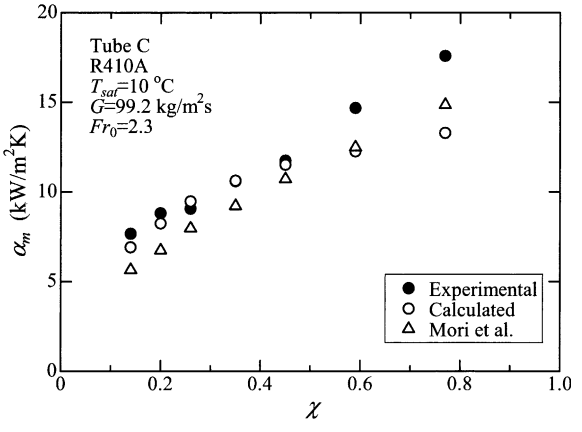

Fig. 13. Comparison of measured and predicted α_m values.

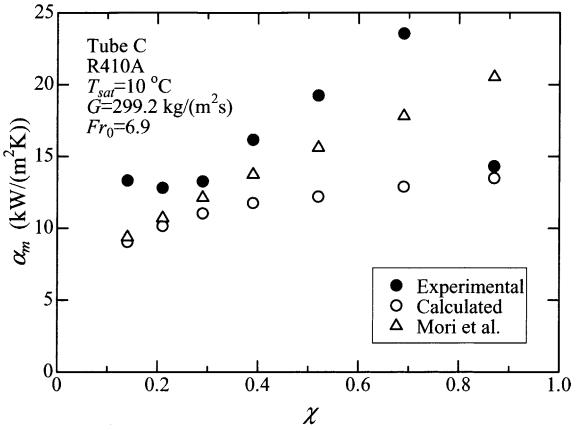

Fig. 14. Comparison of measured and predicted α_m values.

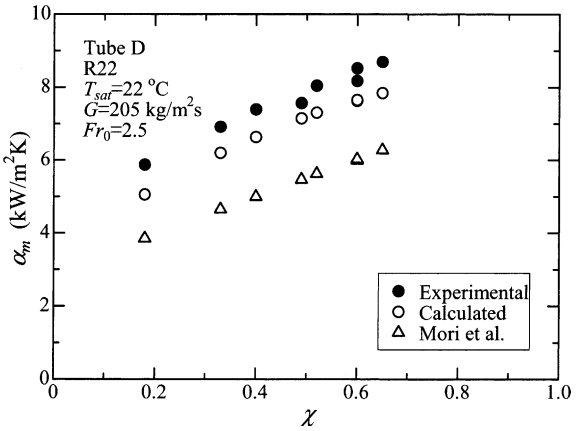

Fig. 15. Comparison of measured and predicted α_m values.

good for $\chi < 0.3$ but the theoretical prediction gives increasingly smaller value than the measurement for $\chi > 0.3$. Figs. 11 and 12 show the cases of tube B with R410A at $G = 98.1$ and 295.5 kg/m^2 s, respectively. The trend of the data is basically the same as the cases of Figs. 8 and 9 but theoretical prediction is much lower than the measurement for Figs. 11 and 12. In Fig. 11, while the measured α_m shows an abrupt decrease (from 14.76 to 6.14 kW/m^2 K) as χ changes from 0.66 to 0.82, the calculated α_m shows a large increase (from 14.08 to 18.50 kW/m^2 K) in the same region. The decrease in the measured value is due to the partial dry out of tube surface, which results in a large decrease in q_m (from 19.8 to 14.4 kW/m^2) and an abrupt increase in $T_s - T_{wm}$ (from 1.36 to 3.24 K). The increase in the calculated α_m is due to the increase in both α_1 (from 15.0 to 20.6 kW/m^2 K) and α_2 (from 12.6 to 14.5 kW/m^2 K). The former is caused by the decrease in $q_1 (= q_m)$ and a moderate increase in φ_s (from 120.7° to 131.2°). The latter is caused by an increase in the liquid velocity. In Fig. 12, the calculated α_m increases only slightly (from 12.2 to 12.7 kW/m^2 K) as changes from 0.70 to 0.89. This is due to

the fact that the decrease in q_m is very small (from 63.2 to 62.1 kW/m^2). Figs. 13 and 14 show the cases of tube C with R410A at $G = 99.2$ and 299.2 kg/m^2 s, respectively. The agreement between the measured and calculated values is good for Fig. 13 though the theoretical prediction deviates toward a smaller value for $\chi > 0.6$. In Fig. 14, the trend of the data is basically the same as the case of Fig. 9. Fig. 15 shows the case of tube D with R22 at $G = 205$ kg/m^2 s. The calculated value is about 10% lower than the experimental data for the whole range of χ.

Since the present theoretical model is based on the assumption of stratified flow, applicability of the numerical results depends on the flow pattern in the tube. According to Taitel and Dukler [19], the boundary between the stratified-wavy flow and the annular/intermittent flows is given by a broad band plotted on the coordinates of $Fr = G\chi/\sqrt{d_e g\rho_v(\rho_l - \rho_v}$ vs. X_{tt}. Since the flow pattern change in the evaporator tube proceeds along a curve which is nearly parallel to the above boundary, the dimensionless quantity $Fr_0 = G/\sqrt{gd_e\rho_v(\rho_l - \rho_v)}$ may be used as a measure for determining the applicability of the present theoretical model. In Figs. 8–15, the value of Fr_0 is also shown. Comparison of these figures reveals that the present theoretical model gives a good prediction of α_m for $Fr_0 < 2.5$ as long as the partial dry out of the tube does not occur. However, the theory underpredicts the measured value for $Fr_0 > 4.0$ and the difference between the two increases with Fr_0. In this region, an annular flow model similar to that previously developed for condensation in horizontal microfin tubes [13] will be applicable.

4. Conclusions

The stratified flow model of evaporation heat transfer in horizontal microfin tubes have been developed. The profile of stratified liquid was determined by the combination of modified Taitel and Dukler model [19] for the void fraction and the Brauner et al. model [20] for the interface configuration. For the region above the stratified liquid, the meniscus profile in the groove between adjacent fins was determined by a force balance between the gravity and surface tension forces. The thin film evaporation model was applied to predict heat transfer in the thin film region of the meniscus. An iterative method was introduced to obtain the rigorous solution of basic equations for the liquid film thickness under a set of boundary solutions. Heat transfer through the stratified liquid was estimated by using an empirical equation proposed by Mori et al. [12]. Comparison of the prediction of the circumferential average heat transfer coefficient with available experimental data for four tubes and three refrigerants revealed that a good agreement was obtained for $Fr_0 < 2.5$ as long as the partial dry out of tube does not occur. The theory underpredicted the measured value for $Fr_0 > 4.0$ and the difference between the two increased with Fr_0. Previous results for condensation in horizontal microfin tubes [13] suggest that an annular flow model will be applicable to this region.

References

[1] T.A. Newell, R.K. Shah, Refrigerant heat transfer, pressure drop, and void fraction effects in microfin tubes, in: Proceedings of the 2nd International Symposium on Two-Phase Flow and Experimentation, Pisa, Italy, vol. 3, 1999, pp. 1623–1639.

[2] A. Cavallini, D. Del Col, L. Doretti, G.A. Longo, L. Rosetto, Enhanced in tube heat transfer with refrigerants, in: Proceedings of the 20th International Congress of Refrigeration, IIR/IIF, Sydney, Australia, vol. 2, 1999, paper 731.

[3] A. Miyara, H. Takamatsu, S. Koyama, K. Yonemoto, T. Fujii, Forced convective boiling of nonazeotropic refrigerant mixture of R22 and R114 inside a horizontal tube, Trans. JSME Ser. B 54 (1988) 2523–2528.

[4] K. Murata, K. Hashizume, Forced convective boiling of nonazeotropic refrigerant mixtures inside tubes, Trans. ASME J. Heat Transfer 115 (1993) 680–689.

[5] O. Kido, H. Uehara, Correlation for evaporation heat transfer of pure refrigerant inside an internally grooved horizontal tube, Trans. Jpn. Assoc. Refrigerat. 11 (1994) 143–154.

[6] S. Koyama, J. Yu, S. Momoki, T. Fujii, H. Honda, Forced convective flow boiling heat transfer of pure refrigerants inside a horizontal microfin tube, in: Proceedings of the Engineering Foundation Conference on Convective Flow Boiling, Banff, Canada, Taylor & Francis, 1995, pp. 137–142.

[7] K. Murata, A correlation for forced convective boilng heat transfer of binary refrigerant mixtures (2nd report, a spirally grooved tube), Trans. JSME Ser. B 62 (1996) 2723–2728.

[8] S.G. Kandlikar, T. Raykoff, Predicting flow boiling heat transfer of refrigerants in micro-fin tubes, J. Enhanced Heat Transfer 4 (1997) 257–268.

[9] J.R. Thome, N. Kattan, D. Favrat, Evaporation in microfin tubes: a generalizd prediction model, in: Proceedings of the Convective Flow and Pool Boiling Conference, Kloster, Irsee, 1997, paper VII-4.

[10] A. Cavallini, D.A. Del Col, L. Doretti, G.A. Longo, L. Rosetto, Refrigerant vaporization inside enhanced tubes: a heat transfer model, in: Proceedings of the Eurotherm Seminar 62, Grenoble, France, 1998, pp. 222–231.

[11] R. Yun, Y. Kim, K. Seo, H.Y. Kim, A generalized correlation for evaporation heat transfer of refrigerants in micro-fin tubes, Int.J. Heat Mass Transfer 45 (2002) 2003–2010.

[12] H. Mori, S. Yoshida, S. Koyama, A. Miyara, S. Momoki, Prediction of hat transfer coefficients for refrigerants flowing in horizontal, spirally grooved evaporator tubes, in: Proceedings of the 2002 JSRAE Annual Conference, Okayama, Japan, 2002, pp. 547–550.

[13] H.S. Wang, H. Honda, S. Nozu, Modified theoretical models of film condensation in horizontal microfin tubes, Int. J. Heat Mass Transfer 45 (2002) 1513–1523.
[14] H.S. Wang, H. Honda, Condensation of refrigerants in horizontal microfin tubes: comparison of prediction methods for heat transfer, Int. J. Refrigerat. 26 (2003) 452–460.
[15] M. Potash Jr., P.C. Wayner Jr., Evaporation from a two-dimensional extended meniscus, Int.J. Heat Mass Transfer 15 (1972) 1851–1863.
[16] P.C. Stephan, C.A. Busse, Analysis of the heat transfer coefficient of grooved heat pipe evaporator walls, Int.J. Heat Mass Transfer 35 (1992) 383–391.
[17] D. Khrustalev, A. Faghri, Heat transfer during evaporation on capillary-grooved structures of heat pipes, Trans. ASME J. Heat Transfer 117 (1995) 740–747.
[18] J.M. Ha, G.P. Peterson, The interline heat transfer of evaporating thin films along a micro grooved surface, Trans. ASME J. Heat Transfer 118 (1996) 747–755.
[19] Y. Taitel, A.E. Dukler, A model for predicting flow regime transitions in horizontal and near horizontal gas–liquid flow, AIChE J. 22 (1976) 47–55.
[20] N. Brauner, J. Rovinsky, D.M. Maron, Determination of the interface curvature in stratified two-phase systems by energy considerations, Int. J. Multiphase Flow 22 (1996) 1167–1185.
[21] T.C. Carnavos, Heat transfer performance of internally finned tubes in turbulent flow, Heat Transfer Eng. 1 (1980) 32–37.
[22] J.N. Israelachvili, Intermolecular and Surface Forces, second ed., Academic Press, London, 1992.
[23] P.C. Wayner Jr., The effects of interfacial mass transport on flow in thin liquid films, Colloids Surfaces 52 (1991) 71–84.
[24] J. Yu, S. Koyama, S. Momoki, Experimental study of flow boiling heat transfer in a horizontal microfm tube, Reports of Institute of Advanced Material Study Kyushu University 9 (1995) 27–42.
[25] A. Miyara, Y. Otsubo, S. Ohtsuka, Evaporation heat transfer of R410A in herrngbone micro-fin tubes, in: Proceedings of the IIR Conference, Thermophysical Properties and Transfer Processes of New Refrigerants, Paderborn, Germany, 2001, pp. 314–319; also private communication.
[26] D. Del Col, R.L. Webb, R. Narayanamurthy, Heat Transfer mechanisms for condensation and vaporization inside a microfin tube, J. Enhanced Heat Transfer 9 (2002) 25–37.
[27] M.O. McLinden, S.A. Klein, E.W. Lemmon, A.P. Peskin, NIST thermodynamic and transport properties of refrigerants and refrigerant mixtures—REFPROP, version 6.0, 1998.